Generating Arbitrary Superpositions of Nonclassical Quantum Harmonic Oscillator States

S. Saner,* O. Băzăvan, D. J. Webb, G. Araneda, D. M. Lucas, C. J. Ballance, and R. Srinivas†

Department of Physics, Clarendon Laboratory, University of Oxford, Parks Road, Oxford OX1 3PU, United Kingdom

(Received 25 February 2025; revised 27 November 2025; accepted 20 January 2026; published 3 June 2026)

Full coherent control and generation of nonclassical superpositions of the quantum harmonic oscillator are not only of fundamental interest but are crucial for applications in quantum simulations, quantum-enhanced metrology, and continuous-variable quantum computation. Here, we create arbitrary superpositions of nonclassical and non-Gaussian states of a quantum harmonic oscillator using the motion of a trapped ion coupled to its internal spin states. We interleave spin-dependent nonlinear interactions with midcircuit spin measurements that herald the probabilistic preparation of superpositions of squeezed, trisqueezed, and quadsqueezed states, which have not previously been experimentally demonstrated. We achieve independent control over the complex-valued squeezing parameter and the probability amplitude of each constituent, as well as their spatial separation. We directly observe the nonclassical nature of these states in the form of Wigner negativity following a full-state reconstruction. Our methods apply to any system where a quantum harmonic oscillator is coupled to a spin.

DOI: 10.1103/k1xk-yt42

Subject Areas: Atomic and Molecular Physics, Quantum Physics

One of the most fundamental and remarkable aspects of quantum mechanics is superposition, where quantum objects can exist in multiple states simultaneously. This phenomenon was famously described by Schrödinger using the example of a cat that is both dead and alive [1]. Superpositions are not just a curiosity of nature but are central to any application of quantum mechanics. In sensing [2], it is the superposition of two states that respond differently to a given signal, such as a shift in frequency, that enables their use in atomic clocks [3]. In quantum computing, the ability to be in multiple states at once increases the amount of information that can be stored and processed simultaneously and is the basis of quantum advantage [4].

Superpositions of two-level systems can be controlled to almost arbitrary precision in many systems [5–7]. However, they ultimately have only 2 degrees of freedom: the relative amplitude and phase of their complex probabilities, which limits the amount of quantum information and how robustly it can be stored. Creating superpositions of a quantum harmonic oscillator, which is, in contrast, infinite dimensional, has already led to a plethora of resource-efficient error correction protocols [8–10], metrological applications [11], and quantum simulations [12]. Nonetheless, constituents of those superpositions have been limited to two [13–15] or three [16] Fock states, classical states such as coherent states leading to cat states [14,17–20], or Gaussian states such as displaced squeezed states leading to Gottesman-Kitaev-Preskill (GKP) states [8,21–23].

Instead, superpositions between arbitrary squeezed states [24–28], or between non-Gaussian states such as trisqueezed states, exhibit increased Wigner negativities [29,30] and discrete rotational symmetries, which can be a resource for new sensing [31] and error correction schemes [32]. However, the lack of any strong, native interactions that create such superpositions has precluded any experimental realization.

Here, we use a hybrid oscillator-spin system to create such superposition states [24] of the harmonic oscillator; we build on our recent work demonstrating strong spin-dependent nonlinear interactions of the oscillator [33] by incorporating additional single-qubit rotations and midcircuit measurements of the spin. We create an arbitrary combination of generalized squeezed states [34] such as squeezed, trisqueezed, and quadsqueezed harmonic oscillator states. These techniques enable not only arbitrary control of the complex probability amplitudes of the constituents forming the superposition, but also over the interactions that generate them. We can create constituents from interactions of the same type with different strengths and phases or from entirely different nonlinear interactions.

*Contact author: sebastian.saner@physics.ox.ac.uk

†Contact author: raghavendra.srinivas@physics.ox.ac.uk

Published by the American Physical Society under the terms of the Creative Commons Attribution 4.0 International license. Further distribution of this work must maintain attribution to the author(s) and the published article's title, journal citation, and DOI.

The hybrid system is central to our demonstration. Applying the spin-dependent nonlinear interaction to a superposition of spin states leads to an entangled state of the spin and the nonclassical motional states. A midcircuit measurement of the spin disentangles it from the motion, probabilistically projecting the harmonic oscillator into a superposition state, with the measurement outcome heralding which state is prepared. This method enables the repeated application of the nonlinear interaction within a single sequence, as the interaction is unitary and can act on any starting state without destroying it.

We create the spin-dependent nonlinear interaction

$$\hat{H}_k = \frac{\hbar\Omega_k}{2}\hat{\sigma}_z[\hat{a}^k e^{-i\phi} + (\hat{a}^\dagger)^k e^{i\phi}], \tag{1}$$

by combining two noncommuting spin-dependent forces [33,35] (see Appendix A). The spin Pauli operator is defined as $\hat{\sigma}_z = |1_s\rangle\langle 1_s| - |0_s\rangle\langle 0_s|$, while $\hat{a}^\dagger$ ($\hat{a}$) describes the creation (annihilation) operator of a quantum harmonic oscillator. The order of the generalized squeezing interaction [34] is k; setting $k = 2, 3, 4$ generates the squeezing, trisqueezing, and quadsqueezing interactions, respectively. Squeezing interactions have been used extensively in metrology [36,37], while the higher-order trisqueezing [33,38,39] and quadsqueezing [33] create non-Gaussian states of the harmonic oscillator [40]. The coupling strength of the interaction is Ω_k, and ϕ is the phase relative to the oscillator, which also defines the generalized squeezing axis. When applying this interaction to the initial state of the hybrid system $|0_{\mathrm{osc}}, 0_s\rangle$, where $|0_{\mathrm{osc}}\rangle$ represents the harmonic oscillator in its ground state and $|0_s\rangle$ denotes the spin configuration prepared in an eigenstate of $\hat{\sigma}_z$, we obtain a generalized squeezed state $|\zeta_k, 0_s\rangle \coloneqq \exp(-i\hat{H}_k t/\hbar)|0_{\mathrm{osc}}, 0_s\rangle$ with squeezing magnitude $\zeta_k = \Omega_k e^{i\phi} t$.

A superposition between two generalized squeezed states $|\zeta_k\rangle$ and $|-\zeta_k\rangle$, with orthogonal squeezing axes, can be created by applying the sequence shown in Fig. 1(a). Initially, a $R_y(\pi/2)$ rotation brings the spin part of the ion into a superposition state $-|-_s\rangle = (|0_s\rangle - |1_s\rangle)/\sqrt{2}$ before applying the $\hat{\sigma}_z$-conditioned nonlinear coupling. After the nonlinear coupling and another $R_y(\pi/2)$ rotation have been applied, the resulting entangled state of the hybrid system takes the form

$$|\psi\rangle = -N_{k,+}|\psi_{k,+}\rangle|1_s\rangle + N_{k,-}|\psi_{k,-}\rangle|0_s\rangle, \tag{2}$$

where $N_{k,\pm}$ denote the probability amplitudes of the even ($|\psi_{k,+}\rangle$) and odd ($|\psi_{k,-}\rangle$) superpositions of the oscillator, which arise directly from the normalization coefficient of $|\psi_{k,\pm}\rangle = 1/(2N_{k,\pm}) \cdot (|\zeta_k\rangle \pm |-\zeta_k\rangle)$. The normalization coefficients depend on the overlap between $|\zeta_k\rangle$ and $|-\zeta_k\rangle$ and, consequently, on the magnitude and order of the applied nonlinear interaction.

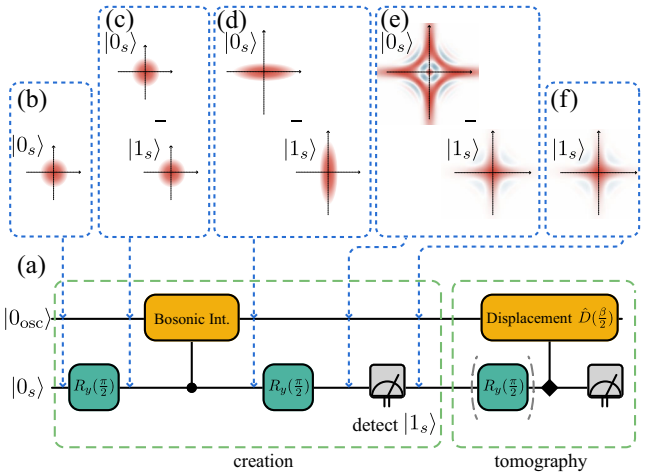


FIG. 1. Quantum circuit for generating superpositions of a quantum harmonic oscillator. We utilize a hybrid system consisting of a harmonic oscillator ($|\mathrm{osc}\rangle$) coupled to a spin ($|0_s\rangle, |1_s\rangle$) [see Fig. 3(b) for the level scheme of the trapped ion used in our implementation]. As an example, we illustrate the creation of a superposition of states squeezed along two different axes (i.e.,$|\zeta_k\rangle$ and $|-\zeta_k\rangle$). However, the same procedure would apply to any other spin-dependent bosonic interaction. (a) Circuit diagram. (b)–(f) The state of the hybrid system at the points of the circuit indicated. At each step, we show the Wigner function of the oscillator state and the corresponding state of the spin. (b) We initialize the hybrid system in $|0_{\mathrm{osc}}, 0_s\rangle$. (c) We first apply a $R_y(\pi/2)$ rotation to the spin qubit to create a superposition of $|0_s\rangle$ and $|1_s\rangle$. (d) After applying the $\hat{\sigma}_z$ spin-conditioned (black dot) bosonic interaction (i.e., generalized squeezing), the oscillator and spin are in an entangled superposition state. (e) The second qubit rotation $R_y(\pi/2)$ brings the hybrid state into a superposition of the form $(|\zeta_k\rangle - |-\zeta_k\rangle)|0_s\rangle$ and $(|\zeta_k\rangle + |-\zeta_k\rangle)|1_s\rangle$, where $|0_s\rangle$ and $|1_s\rangle$ are entangled with the odd and even harmonic oscillator superposition, respectively [see Eq. (2)]. (f) A subsequent measurement projects the state to either the odd or even superposition. We show a projective measurement outcome corresponding to $|1_s\rangle$ that heralds the even superposition. The creation step can be generalized (see Fig. 3) and concatenated (see Fig. 4) to build up arbitrary superposition states. After the creation step (s), we perform state tomography of the final projected oscillator state by measuring the characteristic function of the state [41] and use it to reconstruct the Wigner function. To measure the real part of the characteristic function, we apply a $\hat{\sigma}_y$-conditioned displacement (black diamond) and readout the spin. By adding a $R_y(\pi/2)$ pulse before the conditional displacement, we can measure the imaginary part of the characteristic function instead.

To project into the desired oscillator superposition state, we perform a midcircuit measurement detecting $|0_s\rangle$ or $|1_s\rangle$, which occurs with a probability of $|N_{k,\pm}|^2$. This measurement collapses the state into the corresponding superposition of the oscillator, disentangled from the spin state. After the collapse, the created superposition can be employed in further experiments or characterized through full tomography. Experimentally, we can select the

outcomes with the desired superposition by postselecting based on the midcircuit measurement result.

We experimentally demonstrate the creation of these superpositions on a trapped $^{88}Sr^{+}$ ion in a three-dimensional Paul trap [42,43]. The harmonic oscillator is formed by the axial motion of the confined ion with frequency 1.2 MHz. In practice, we cannot initialize a pure vacuum state of the oscillator $|0_{\mathrm{osc}}\rangle$, but rather a thermal state near its ground state with average occupation $\overline{n} = 0.1$. The coherence time of this oscillator is limited by its heating rate $\dot{\bar{n}} = 300$ quanta/s. The internal structure forms the spin system, with the states $|0_s\rangle \equiv |5S_{1/2}, m_j = -\frac{1}{2}\rangle$, and $|1_s\rangle \equiv |4D_{5/2}, m_j = -\frac{3}{2}\rangle$. The electronic state $|2_s\rangle \equiv |5S_{1/2}, m_j = \frac{1}{2}\rangle$ is used as an auxiliary state.

The $|0_s\rangle \leftrightarrow |1_s\rangle$ quadrupole transition is driven by a 674-nm laser; the two noncommuting spin-dependent forces required to generate the nonlinear interaction are created by two 674-nm beams. The $|2_s\rangle$ state is isolated from the interaction, and an rf antenna drives the $|0_s\rangle \leftrightarrow |2_s\rangle$ transition.

The projective measurement is achieved by driving the $5S_{1/2} \leftrightarrow 5P_{1/2}$ transition that distinguishes bright states ($|0_s\rangle$ or $|2_s\rangle$), which scatter photons, from the dark state ($|1_s\rangle$), which does not. This measurement is nondestructive only to the motional state in the case where $|1_s\rangle$ is detected; hence, no photons are actually scattered. Thus, we design our pulse sequences such that the desired oscillator state is heralded upon $|1_s\rangle$, i.e., the desired harmonic superposition is correlated with $|1_s\rangle$ just before the measurement. For example, for the state described in Eq. (2), we would select the even superposition $|\psi_{k,+}\rangle$. The projective measurement is used midcircuit for selecting the desired superposition as well as for the final detection step. In both cases, we collect photons for 200 μs, yielding a combined dark-state preparation and measurement fidelity of 0.993 (see Appendix B).

We create both even and odd superpositions between the state $|\zeta_k\rangle$ and $|-\zeta_k\rangle$ as illustrated in Eq. (2) and Fig. 1. By measuring the qubit immediately after this creation step, we obtain the probability of collapsing in $|0_s\rangle$ and $|1_s\rangle$, respectively, and, hence, the probability of generating the even and odd superposition. For example, for $k = 2$ in Eqs. (1) and (2), we obtain the superposition between two oscillator states squeezed about orthogonal axes. The corresponding probabilities for the even ($|\psi_{2,+}\rangle$) and odd ($|\psi_{2,-}\rangle$) states are given by $|N_{2,\pm}|^2 = \left(2 \pm 2/\sqrt{\cosh(2|\zeta_2|)}\right)/4$, which depend on the magnitude of the squeezing parameter $|\zeta_2|$ (see Appendix A). In the limit of small squeezing parameter $|\zeta_2|$, the generation of the odd superposition vanishes, which indicates that the overlap between $|\zeta_k\rangle$ and $|-\zeta_k\rangle$ tends to 1 as the oscillator state is unchanged from the initial state. In the limit $|\zeta_2| \to \infty$, the odd and even state have equal generation probability of 1/2, which indicates that $|\zeta_2\rangle$ and $|-\zeta_2\rangle$ are orthogonal and their overlap is 0. We confirm this behavior experimentally; the data in Fig. 2(a) agree well with the theoretical prediction from an independent estimate of $|\zeta_2|$.

Extending this protocol to higher-order nonlinear interactions, we reconstruct the Wigner quasiprobability distribution of even and odd superpositions for squeezing ($k = 2$), trisqueezing ($k = 3$), and quadsqueezing ($k = 4$)

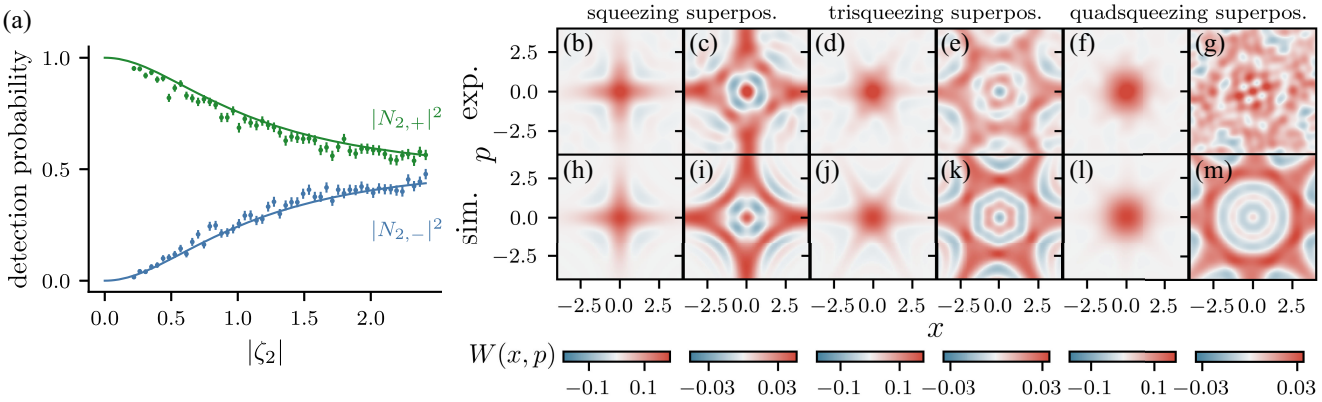


FIG. 2. Equal superpositions of generalized squeezed states. (a) Probability of creating even (green dots) and odd (blue dots) squeezed superposition states $|\psi_{2,\pm}\rangle = 1/(2N_{2,\pm}) \cdot (|\zeta_2\rangle \pm |-\zeta_2\rangle)$ as a function of the squeezing magnitude $|\zeta_2|$. The theoretical detection probability values $|N_{\pm}|^2$ predicted by the coefficients in Eq. (2) are displayed as solid lines. At large values of $|\zeta_2|$, the detection probabilities $|N_{2,\pm}|^2$ approach 0.5. Error bars denote the 68% confidence interval. (b)–(g) Experimentally reconstructed Wigner functions of even and odd superpositions $|\psi_{k,\pm}\rangle = 1/(2N_{k,\pm}) \cdot (|\zeta_k\rangle \pm |-\zeta_k\rangle)$ shown for squeezed, trisqueezed, and quadsqueezed superpositions. The estimated squeezing magnitudes are $|\zeta_2| \approx \{1.12(5), 1.67(7)\}$ for squeezed (b),(c), $|\zeta_3| \approx \{0.74(5), 0.74(5)\}$ for trisqueezed (d),(e), and $|\zeta_4| \approx \{0.059(5), 0.16(1)\}$ for quadsqueezed (f),(g) superpositions. The experimental parameters are tabulated in Appendix B. For the odd states of the squeezed and quadsqueezed superpositions, we have increased the squeezing magnitude relative to the even state to highlight the interference effects. (h)–(m) Simulated Wigner function of (b)–(g) using independently measured experimental parameters.

[Figs. 2(b)–2(g)]. To do so, we measure the characteristic function $\chi(\beta) = \langle \hat{D}(\beta) \rangle_{\mathrm{osc}}$ of the oscillator state and infer the Wigner distribution via a Fourier transform [33,41]. The characteristic function $\chi(\beta)$ is measured via the spin using a spin-dependent displacement $\hat{D}(\hat{\sigma}_y \beta/2)$, as shown in the tomography step in Fig. 1(a). By varying the complex-valued displacement parameter β, we can sample different values of $\chi(\beta)$ (see Appendix C). We also provide numerical simulations using independently measured parameters, which account for both the initial thermal state and the heating rate [Figs. 2(h)–2(m)]. While identifying the most appropriate metric for analyzing such states, particularly when they are mixed, remains an open question, we calculate the Hilbert-Schmidt fidelity between the experimental data and numerical simulations (see Appendix C). The fidelity shows good agreement in all cases except Figs. 2(g) and 2(m); however, it should be interpreted with care: High fidelity does not ensure all quantitative details are captured perfectly, and lower fidelity does not imply a loss of essential qualitative structure. Indeed, central features such as the eightfold rotational symmetry and ringlike interference pattern remain visible in all cases. These results highlight the need for state-quality metrics beyond single-number measures to fully characterize the richness and complexity of the states now experimentally accessible. Further, we show the corresponding numerical predictions of $|N_{k,\pm}|^2$ as a function of $|\zeta_k|$ for $k \in 3, 4$, plotted alongside the experimental data, and discuss that, for Figs. 2(g) and 2(m), midcircuit detection errors become comparable to the herald probability.

The superpositions created, especially the odd ones, have a large amount of Wigner negativity. In continuous-variable quantum computation, large Wigner negativities are a requirement for quantum states that yield an advantage over classical computation [44,45] and hence are highly sought after. We quantify the resourcefulness of these states by evaluating their Wigner logarithmic negativity (WLN) [29,30], neglecting decoherence effects, and benchmark them against Fock and cat states. We find that, for a fixed average Fock-state occupation, the superpositions created in this work exhibit larger WLN than Fock or cat states [46] (see Appendix C).

Another important feature is that the nonvanishing Fock-state occupations of the superpositions are spaced by $2k$, where k is the order of the interaction (see Appendix C). As k increases, so does the spacing, and the states have increased rotational symmetries as seen in Fig. 2. These rotational symmetries can be used to encode more robust logical qubits [32]. For example, a single phonon loss in a (two-component) cat-state qubit encoding results in an irreparable bit-flip error [17]. However, when the same loss channel acts on a qubit encoding formed by a superposition of squeezed states, it projects outside the code space, making the error correctable.

Thus far, the superpositions have involved only constituents generated from the same nonlinear interactions.

To create arbitrary superpositions with nonclassical constituents in the most general form

$$|\psi\rangle \propto a|\zeta_k\rangle + b|\zeta_{k'}\rangle, \tag{3}$$

we require individual control of $a, b, \zeta_k, \zeta_{k'} \in \mathbb{C}$. To create this state, we extend the Hilbert space of the spin to a qutrit (three-level system), $\{|0_s\rangle, |1_s\rangle, |2_s\rangle\}$ [see Figs. 3(a) and 3(b)]. We create the constituent states via the same interaction described in Eq. (1), which couples only to $|0_s\rangle$ when applied to the subspace $\{|0_s\rangle, |2_s\rangle\}$. Thus, we utilize this feature to temporarily hide one of the constituents $|\zeta_k, 2_s\rangle$, while creating the other using a separate interaction [47].

The pulse sequence for creating the arbitrary superpositions is described in Fig. 3(a); for simplicity, we first focus on the case $a = b$. After the first nonlinear interaction is applied, the hybrid system is in a state $-|0_{\mathrm{osc}}, 2_s\rangle + |\zeta_k, 0_s\rangle$. A subsequent $R_y(\pi)_{02}$ rotation, where the indices indicate the two spin sublevels $|0_s\rangle \leftrightarrow |2_s\rangle$ coupled, then swaps the spin states, hiding the state $|\zeta_k, 2_s\rangle$ from the effect of the second nonlinear interaction. The second nonlinear interaction then creates the state $|\zeta_k, 2_s\rangle + |\zeta'_{k'}, 0_s\rangle$. One final $R_y(\pi/2)_{02}$ pulse followed by the shelving $R_y(\pi)_{01}$ pulse creates a state similar to the state described by Eq. (2), with $|\psi_{k,\pm}\rangle \propto |\zeta_k\rangle \pm |\zeta'_{k'}\rangle$, where $\zeta'_{k'}$ is no longer $-\zeta_k$.

We then characterize the state using the same techniques as before. As mentioned previously, the unitarity of the nonlinear interaction is essential to prevent the destruction of the intermediate state by subsequent applications of the nonlinear interaction. Splitting the sequence into two parts allows us to change the second nonlinear interaction relative to the first one [48].

In Fig. 3(c), we show that we can create a superposition of squeezed states with variable orientation of the respective squeezing axis, i.e., $\zeta'_2 = e^{i2\phi}\zeta_2$, by adjusting the phase ϕ of the nonlinear interaction in the second part of the sequence relative to the first part. Hence, the created state takes the form $|\zeta_2\rangle + |e^{i2\phi}\zeta_2\rangle$. We measure the value of the characteristic function at a fixed magnitude $|\beta|$, but vary its complex phase $\arg(\beta)$. At $\phi = \pi/2$, we create a superposition of states squeezed about orthogonal axes [equal superposition of squeezed states shown in Figs. 2(b) and 2(h)], which gives rise to four equally spaced maxima in χ when scanning $\arg(\beta)$. By scanning the degree of freedom ϕ, the two orthogonal squeezing axes gradually merge into a single one at $\phi = \{0, \pi\}$ (regular squeezed state), giving rise to two equally spaced maxima. This behavior results in the sawtooth pattern displayed in Fig. 3(c).

In Fig. 3(d), we show that we can control the magnitude of squeezing of each constituent independently [49]. We keep the squeezing parameter ζ_2 of the first constituent

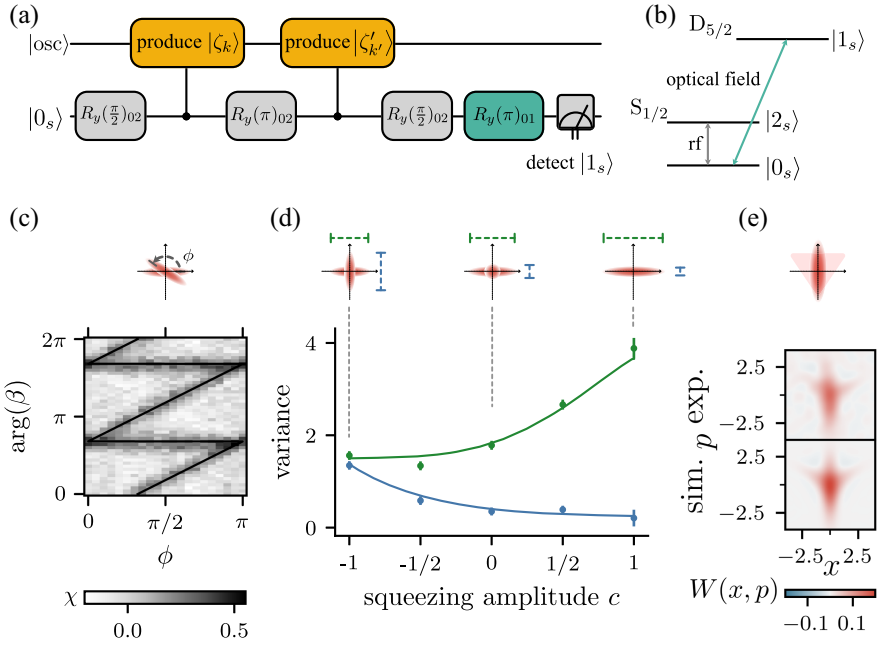


FIG. 3. Generation of superpositions with arbitrary constituents. (a) The sequence used to create these superpositions is similar to Fig. 1(a), but extended to a qutrit system such that the constituents ($|\zeta_k\rangle$, $|\zeta'_{k'}\rangle$) can be produced sequentially. The indices next to the rotations $R_y()_{ij}$ and colors indicate the two spin sublevels $|i\rangle \leftrightarrow |j\rangle$ coupled. (b) Level diagram of the three-level spin system, using both levels of the ground $S_{1/2}$ state and one level in the excited $D_{5/2}$ state. We use radio frequency (rf) pulses to perform rotations between $|0_s\rangle \leftrightarrow |2_s\rangle$, and optical fields for rotations between $|0_s\rangle \leftrightarrow |1_s\rangle$. The bosonic interaction is performed by optical fields and, hence, couples only the $|0_s\rangle$ and $|1_s\rangle$ states. (c) We first create superposition states with the same squeezing amplitude, but arbitrary phase ϕ, i.e., $|\zeta_2\rangle + |e^{i2\phi}\zeta_2\rangle$. To verify control over ϕ and, consequently, the angle between the squeezing axes of the two constituents, we measure the value of the characteristic function $\chi(\beta)$ at a fixed magnitude $|\beta|$, but vary its complex argument $\arg(\beta)$. Maxima in χ indicate the location of squeezing axes of the two constituents. The estimated squeezing magnitude is $|\zeta_2| = 1.12(5)$. (d) We next vary the squeezing amplitude between the states, i.e., $|\zeta_2\rangle + |c \cdot \zeta_2\rangle$ and measure the variance of the state along x (green) and p (blue) for various settings of c. Error bars denote the 68% confidence interval via bootstrapping. Solid lines denote the numerically simulated value for the variance. (e) We show the experimentally reconstructed Wigner function of an even superposition state between a squeezed and trisqueezed state $|\zeta_2\rangle + |\zeta_3\rangle$ (upper row) as well as the simulated Wigner function (lower row). The squeezing and trisqueezing magnitudes are $\zeta_2 \approx 1.12(5)$ and $\zeta_3 \approx 0.25(2)$, respectively. The insets show the Wigner function of each of the constituents overlapped to illustrate the expected resulting Wigner functions. The insets do not depict the coherences between the two constituents, which are present in the real superposition states. The experimental parameters are tabulated in Appendix B.

fixed, while adjusting the magnitude of the second constituent by a factor $c \in \mathbb{R}$, which results in a state $|\zeta_2\rangle + |c \cdot \zeta_2\rangle$, i.e., $\zeta'_2 = c\zeta_2$. For $c = 0$, this corresponds to a superposition of a squeezed state with the initial ground state, whereas for $c = -1$, this corresponds to the equal superposition shown in Figs. 2(b) and 2(h). We measure the variance of the state along the squeezing axis of the first constituent and an axis orthogonal to it (i.e., two orthogonal quadratures). We compute the variances using the reconstructed Wigner functions for different settings of c. As shown in Fig. 3(d), the variance closely follows the simulated prediction.

The variance of each constituent does not vary independently. In fact, altering the magnitude of the second constituent affects the variance of the resulting state in both quadratures: the quadrature dominated by the second constituent (blue) and the quadrature dominated by the first constituent (green), even though the first constituent's squeezing magnitude remains fixed. This behavior is a direct consequence of the interference between both constituents.

To demonstrate that we can change the order k of the nonlinear interaction for each constituent, we combine a squeezed state ($k = 2$) as the first constituent with a trisqueezed state ($k = 3$) as the second constituent. Figure 3(e) shows the resulting Wigner function of this superposition state. While we do not include the data in the main text, we discuss in Appendix A that the sequence can be amended to vary the relative amplitude and phase of the probability coefficients a and b. By replacing the first $R_y(\pi/2)$ rotation with $R_y(\theta)$, it is possible to vary the probability amplitude ratio between the two constituents, $[\cos(\theta/2)|\zeta_k\rangle + \sin(\theta/2)|-\zeta_k\rangle]$. Further, it is also possible to replace the $R_y(\pi)$ rotation with a rotation about an axis $\hat{\sigma}_\gamma = \cos(\gamma)\hat{\sigma}_x + \sin(\gamma)\hat{\sigma}_y$ to introduce a complex phase factor between the probability amplitude of the

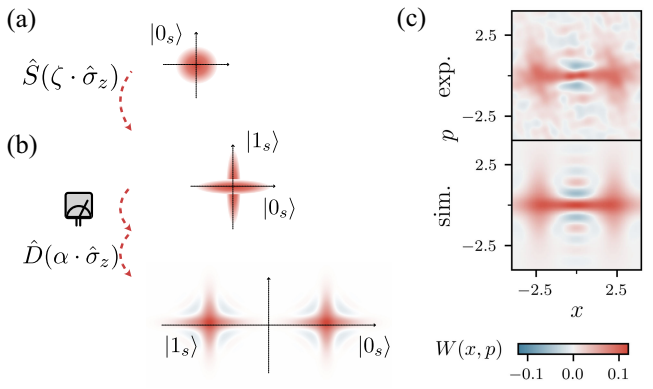


FIG. 4. Constructing arbitrary cat states with multiple midcircuit measurements. (a),(b) We illustrate the main steps under which the initial state $|0_{\mathrm{osc}}, 0_s\rangle$ is transformed. For simplicity, we omit the single-qubit rotations before each detection. (a) The first step is the same as in Fig. 2(a). The hybrid system is brought into an equal superposition of squeezed states entangled with the spin. (b) After a successful detection step, we obtain the motional state $|\psi_{2,+}\rangle = |\zeta_2\rangle + |-\zeta_2\rangle$ that is no longer entangled with the spin and we can apply a second spin-conditioned operation. As an example, we choose a spin-dependent displacement, which, after a second midcircuit step, creates a state reminiscent of a cat state where each of the cat state constituents is formed by a squeezed superposition displaced in opposite directions. (c) Experimental and simulated Wigner function of this ψ_+-cat state. The estimated squeezing magnitude is $|\zeta_2| = 1.25(4)$ followed by the displacement magnitude $|\alpha| = |\zeta_1|/2 = 1.62(4)$. The displacement axis is aligned with one of the squeezing axes. The experimental parameters are tabulated in Appendix B.

two constituents $|\zeta_k\rangle + |-\zeta_k\rangle e^{i2\gamma}$. Thus, we demonstrate complete control over a, b, ζ_k, and $\zeta'_{k'}$ in Eq. (3).

Finally, we show that the sequence depicted in Fig. 1(a) can be extended further to construct spatially separated superposition states. Aside from a foundational quantum optics interest, such spatially separated superpositions are essential in various applications, including continuous-variable quantum error correction codes (e.g., cat [17] or GKP [8] states) and metrology [50]. We create these states using an additional spin-dependent displacement followed by a midcircuit measurement as shown in Fig. 4. The second midcircuit detection disentangles the spin from the harmonic oscillator, projecting the latter into a catlike state, where the two spatially displaced states are themselves nonclassical and non-Gaussian. We use this protocol to create a spatially separated superposition of squeezed states

$$|\psi\rangle \propto D(\alpha)|\psi_{2,+}\rangle + D(-\alpha)|\psi_{2,+}\rangle, \tag{4}$$

where $|\psi_{2,+}\rangle \propto |\zeta_2\rangle + |-\zeta_2\rangle$. A slight skew is visible in the experimental Wigner function, likely due to a minor miscalibration in Fig. 4(b), but the overall agreement with the simulation is good. The two displaced $|\psi_{2,+}\rangle$ components and their interference fringes are clearly visible in both. The calculated fidelity between experiment and numerical simulation confirms this agreement (see Appendix C). Thus, we show that we can create an even broader class of oscillator superpositions by concatenating additional spin-dependent interactions and midcircuit measurements.

Our work demonstrates the versatility of hybrid oscillator-spin systems in probabilistically generating heralded superpositions of oscillator states. By integrating nonlinear spin-dependent interactions with midcircuit measurements, we have established arbitrary control of the phase, amplitude, and interaction type for the constituents of the superpositions. Using these techniques, we have experimentally demonstrated many nonclassical states that have until now been only explored theoretically [24–26,28,31].

Expanding complex harmonic oscillator states from cat [17] and GKP [8] states to superpositions of squeezed or superpositions of non-Gaussian states is not only of foundational interest, but opens new avenues for error correction, sensing protocols, and continuous-variable or hybrid oscillator-spin quantum computing [51]. For example, these superposition states have increased rotational symmetries, which enable robust error correction [32]. Further, their large Wigner negativities indicate that they generally cannot be efficiently simulated classically [44,45]. Their utility applies not only to quantum computation, but also to quantum-enhanced metrology. For example, the squeezed superposition state is suitable as a displacement sensor [31], which, in the case of trapped ions, can be used for sensing small electric fields [50]. The demonstrated techniques can be extended to multiple oscillators by coupling to additional motional modes of the ion; for example, to create two-mode squeezed superpositions [52] or, in general, to increase the size of the hybrid quantum system. Aside from trapped ions, the tools developed here can be applied to any physical system with a quantum harmonic oscillator coupled to a spin (see Appendix A), such as superconducting circuits [53], nanoparticles [54], or atoms coupled to a cavity [55] or in optical tweezers [56]. For systems with more massive oscillators, these superpositions could be used to test not only the boundaries of the classical and quantum world [57], but how quantum physics interacts with gravity [58].

We would like to thank Alejandro Bermudez, Alexander Lvovsky, Andrew Daley, Joshua Combes and his research group, Mattia Walschaers, and Scott Parkins for very insightful discussions and comments on the manuscript. This work was supported by the U.S. Army Research Office (W911NF-20-1-0038) and the UK EPSRC Hub in Quantum Computing and Simulation (EP/T001062/1). G. A. acknowledges support from Wolfson College, Oxford. C. J. B. acknowledges support from a UKRI FL Fellowship. R. S. acknowledges funding from the EPSRC Fellowship EP/W028026/1 and Balliol College, Oxford.

S. S. and O. B. led the experiments and analyzed the results with assistance from D. J. W., G. A., and R. S.; S. S., O. B., D. J. W., and G. A. updated and maintained the experimental apparatus; S. S., O. B., and R. S. conceived the experiments and wrote the manuscript with input from all authors; R. S. supervised the work with support from D. M. L. and C. J. B.; D. M. L. and C. J. B. secured funding for the work.

R. S. is partially employed by Oxford Ionics, Ltd. C. J. B. is a director of Oxford Ionics, Ltd. All other authors declare no competing interests.

DATA AVAILABILITY

The data that support the findings of this article are not publicly available upon publication because it is not technically feasible and/or the cost of preparing, depositing, and hosting the data would be prohibitive within the terms of this research project. The data are available from the authors upon reasonable request.

APPENDIX A: THEORY

1. Generating the nonlinear spin-dependent interaction

While the method employed to generate the nonlinear interaction is described in detail in Refs. [33,35]. We summarize the relevant details below. We combine two spin-dependent forces (SDFs) with noncommuting spin conditionings $[\hat{\sigma}_\alpha, \hat{\sigma}_{\alpha'}] \neq 0$ and ϕ the oscillator phase of the second SDF, which results in a Hamiltonian

$$\hat{H} = \frac{\hbar\Omega_\alpha}{2}\hat{\sigma}_\alpha(\hat{a}e^{-i\Delta t} + \hat{a}^\dagger e^{i\Delta t}) + \frac{\hbar\Omega_{\alpha'}}{2}\hat{\sigma}_{\alpha'}(\hat{a}e^{-i(m\Delta t+\phi)} + \hat{a}^\dagger e^{i(m\Delta t+\phi)}). \tag{A1}$$

The two forces are detuned from resonance with the oscillator by Δ and $m\Delta$, respectively. By choosing $k = 1 - m$, we can resonantly drive effective generalized squeezing interactions

$$\hat{H}_k = \frac{\hbar\Omega_k}{2}\hat{\sigma}_\beta[\hat{a}^k e^{-i\phi} + (\hat{a}^\dagger)^k e^{i\phi}], \tag{A2}$$

which for $\hat{\sigma}_\beta = \hat{\sigma}_z$ corresponds to Eq. (1) in the main text, where

$$\hat{\sigma}_\beta \propto \begin{cases} [\hat{\sigma}_\alpha, \hat{\sigma}_{\alpha'}] & \text{if } k \bmod 2 = 0, \\ \hat{\sigma}_{\alpha'} & \text{otherwise.} \end{cases} \tag{A3}$$

While we can choose our spin bases such that $\hat{\sigma}_\beta = \hat{\sigma}_z$, and do so for the majority of the data, it was convenient for Figs. 2(d) and 2(e) to choose $\hat{\sigma}_\beta = \hat{\sigma}_x$, which maximizes the strength and avoids two single-qubit rotations. We have indicated the native spin conditioning for every sequence in B 1. The coupling strength Ω_k,

$$\Omega_{2,3,4} = \left\{\frac{\Omega_{\alpha'}\Omega_\alpha}{\Delta}, \frac{\Omega_{\alpha'}\Omega_\alpha^2}{2\Delta^2}, \frac{\Omega_{\alpha'}\Omega_\alpha^3}{8\Delta^3}\right\} \cdot \sin(\theta_{\alpha,\alpha'}), \tag{A4}$$

which is proportional to $\sin(\theta_{\alpha,\alpha'})$, where $\theta_{\alpha,\alpha'}$ denotes the angle between the spin bases α and α' and is maximized if the two spin bases are orthogonal. We utilize this angle to adjust the squeezing magnitude for the constituent $|c \cdot \zeta_2\rangle$ in the superposition of Fig. 3(d), while keeping the optical power and the duration of the interaction fixed. For the quantum circuits presented in the main text, we adjust Δ, Ω_α, $\Omega_{\alpha'}$, and $\hat{\sigma}_\beta$. The settings are tabulated in B 1.

2. Normalization coefficient

We require the squeezed-state superposition to be normalized, i.e., $\langle\psi_\pm|\psi_\pm\rangle = 1$, and find a normalization coefficient

$$\begin{aligned} |N_{2,\pm}|^2 &= \frac{1}{4}(\langle\zeta_2| \pm \langle\zeta_2|)(|\zeta_2\rangle \pm |\zeta_2\rangle) \\ &= \frac{1}{4}\langle\zeta_2|\zeta_2\rangle + \langle-\zeta_2| - \zeta_2\rangle \pm 2\mathrm{Re}(\langle-\zeta_2|\zeta_2\rangle) \\ &= \left(2 \pm \frac{2}{\sqrt{\cosh(2|\zeta_2|)}}\right)\Big/4, \end{aligned} \tag{A5}$$

where we assume that each squeezed state is normalized. The inner product $\langle-\zeta_2|\zeta_2\rangle$ can be determined from the Fock-state expression of a vacuum squeezed state [59–61],

$$|\zeta_2\rangle = \frac{1}{\sqrt{\cosh(|\zeta_2|)}}\sum_{n=0}^{\infty}[-e^{i\arg(\zeta_2)}\tanh(|\zeta_2|)]^n\frac{\sqrt{(2n)!}}{2^n n!}|2n\rangle, \tag{A6}$$

$$\begin{aligned} \langle-\zeta_2|\zeta_2\rangle &= \frac{1}{\cosh(|\zeta_2|)}\sum_{n=0}^{\infty}e^{i\pi n}\tanh(|\zeta_2|)^{2n}\frac{(2n)!}{2^{2n}(n!)^2} \\ &= \frac{1}{\cosh(|\zeta_2|)}\frac{1}{\sqrt{\tanh(|\zeta_2|)^2+1}} = \frac{1}{\sqrt{\cosh(2|\zeta_2|)}}. \end{aligned} \tag{A7}$$

For the superpositions involving non-Gaussian (i.e., trisqueezed or quadsqueezed) constituents, it is unclear if closed-form solutions exist [34].

3. Native gate sequences

In this section, we give a more detailed description of the pulse sequence used to generate the superposition states. For simplicity, we omitted the spin-echo $R(\pi)$ pulses described below from the main text and Fig. 1.

All nonlinear interactions $\hat{U}_{\mathrm{NL}}$ except for trisqueezing in Fig. 2 are conditioned on $\hat{\sigma}_z = |1_s\rangle\langle 1_s| - |0_s\rangle\langle 0_s|$.

For squeezing and quadsqueezing, we set $\hat{\sigma}_\alpha = \sigma_x$ and $\sigma_{\alpha'} = \hat{\sigma}_y$, which results in $\hat{\sigma}_\beta = \hat{\sigma}_z$. For the trisqueezing superposition shown in Fig. 2, we keep this setting, which results in the spin basis of the nonlinear interaction $\hat{\sigma}_\beta = \hat{\sigma}_x$. For trisqueezing shown in Fig. 3, we change the trisqueezing spin basis compared to Fig. 2. We set the spin conditioning of the SDF to $\hat{\sigma}_{\alpha'} = \hat{\sigma}_z$, such that the resulting nonlinear interaction is conditioned on $\hat{\sigma}_\beta = \hat{\sigma}_z$,

$$|0_{\mathrm{osc}}, 0_s\rangle \xrightarrow{R_y(\pi/2)} \frac{|0_{\mathrm{osc}}, 0_s\rangle - |0_{\mathrm{osc}}, 1_s\rangle}{\sqrt{2}} \xrightarrow{\hat{U}_{\mathrm{NL}}} \frac{|\zeta/2, 0_s\rangle - |-\zeta/2, 1_s\rangle}{\sqrt{2}}, \tag{A8}$$

$$\xrightarrow{R_y(\pi)} \frac{-|\zeta/2, 1_s\rangle - |-\zeta/2, 0_s\rangle}{\sqrt{2}} \xrightarrow{\hat{U}_{\mathrm{NL}}|_\pi} \frac{-|\zeta, 1_s\rangle - |-\zeta, 0_s\rangle}{\sqrt{2}}, \tag{A9}$$

$$\xrightarrow{R_y(\pi/2)} -N_+(|\zeta\rangle + |-\zeta\rangle)|0_s\rangle - N_-(|\zeta\rangle - |-\zeta\rangle)|1_s\rangle. \tag{A10}$$

We can adjust the phases of the qubit rotations to adjust which harmonic oscillator superposition is heralded by $|1_s\rangle$. For example, we can change the axis of the $R_y(\pi)$ pulse to $R_x(\pi)$. The sequence continued from Eq. (A8) then looks like

$$\xrightarrow{R_x(\pi)} \frac{-i|\zeta/2, 1_s\rangle + i|-\zeta/2, 0_s\rangle}{\sqrt{2}} \xrightarrow{\hat{U}_{\mathrm{NL}}|_\pi} \frac{-i|\zeta, 1_s\rangle + i|-\zeta, 0_s\rangle}{\sqrt{2}}, \tag{A11}$$

$$\xrightarrow{R_y(\pi/2)} -iN_-(|\zeta\rangle - |-\zeta\rangle)|0_s\rangle - iN_+(|\zeta\rangle + |-\zeta\rangle)|1_s\rangle. \tag{A12}$$

For the trisqueezing superposition shown in Fig. 2, we omit the $R(\pi/2)$ and $R(\pi)$ pulses. To herald the even (odd) superposition upon detecting $|1_s\rangle$, we initialize the starting state in $|1_s\rangle$ ($|0_s\rangle$) before applying the interaction.

For the sequence in Fig. 3, we require all of the applied nonlinear interaction to be conditioned on $\hat{\sigma}_z$, such that we can treat its impact on the subsystem $\{|0_s\rangle, |2_s\rangle\}$ as a closed system.

4. Adjusting the probability amplitude coefficient of the superpositions

We can arbitrarily set the probability amplitudes of each constituent instead of only balanced superpositions. To adjust the relative amplitudes, we can replace the first $R_y(\pi/2)$ rotation by a $R_y(\theta)$ rotation, such that the initial spin superposition is of the form

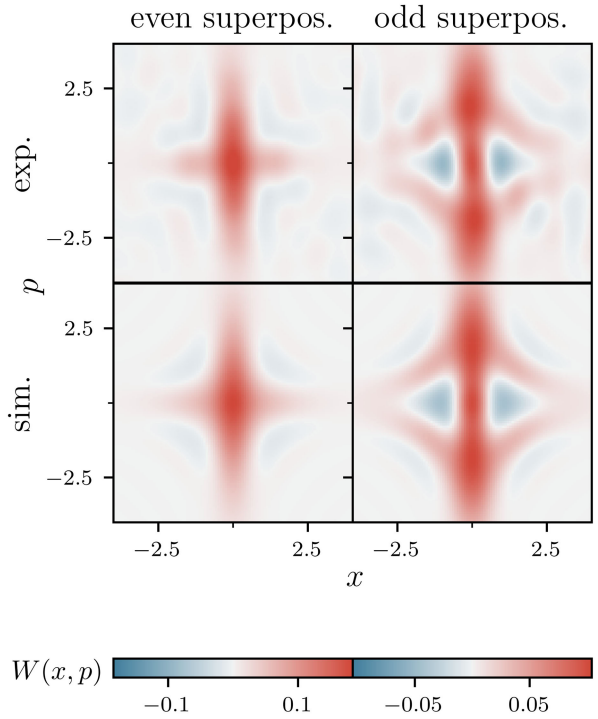


FIG. 5. Wigner function of the state $|\psi\rangle \propto a|\zeta_2\rangle \pm b|-\zeta_2\rangle$ with a probability amplitude ratio $a/b = \cos(\theta/2)/\sin(\theta/2) = \sqrt{2}+1$, where $\theta = \pi/4$. We show experimental and numerical simulation data for both even (+) and odd (-) superpositions. We choose $|\zeta_2| = 1.12(5)$, consistent with Fig. 2(b).

$$|\psi\rangle = \cos(\theta/2)|0_{\mathrm{osc}}, 0_s\rangle - \sin(\theta/2)|0_{\mathrm{osc}}, 1_s\rangle. \tag{A13}$$

The rest of the sequence remains unchanged. This results in an amplitude ratio $\cos(\theta/2)/\sin(\theta/2)$ between the constituents of the superposition. For example, for $\theta = \pi/2$, the amplitudes are equal and the sequence is the same as in Eq. (A8). As a proof of principle, we produce a squeezed-state superposition with $\theta = \pi/4$, i.e., $a|\zeta_2\rangle + b|-\zeta_2\rangle$ with an amplitude ratio $a/b = \sqrt{2}+1$ (see Fig. 5).

To adjust the relative phase of the complex probability amplitudes, we vary the axis $\hat{\sigma}_\gamma = \cos(\gamma)\hat{\sigma}_x + \sin(\gamma)\hat{\sigma}_y$ of the $R_\gamma(\pi)$ rotation. After the full sequence, we obtain

$$|\psi\rangle = -N_+^{(\gamma)}(|\zeta\rangle ie^{-i\gamma} - |-\zeta\rangle ie^{i\gamma})|0_s\rangle - N_-^{(\gamma)}(|\zeta\rangle ie^{-i\gamma} + |-\zeta\rangle ie^{i\gamma})|1_s\rangle. \tag{A14}$$

After rearranging, we obtain

$$|\psi\rangle = -ie^{-i\gamma}N_+^{(\gamma)}(|\zeta\rangle - |-\zeta\rangle e^{i2\gamma})|0_s\rangle - ie^{-i\gamma}N_-^{(\gamma)}(|\zeta\rangle + |-\zeta\rangle e^{i2\gamma})|1_s\rangle. \tag{A15}$$

For $\gamma = \pi/2$, this reduces to Eq. (A10) with $N_\pm^{(\pi/2)} = N_\pm$, whereas for $\gamma = 0$ it reduces to Eq. (A12) with $N_\pm^{(0)} = N_\mp$.

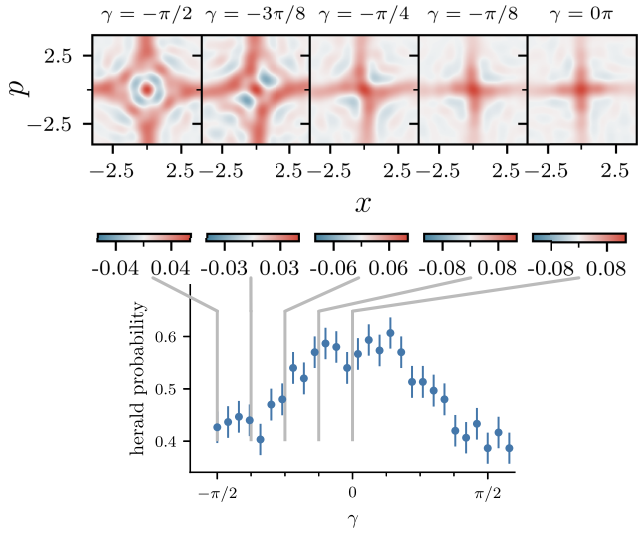


FIG. 6. Measuring the herald probability $|N_+^{(\gamma)}|^2$ and the resulting Wigner functions of the state $|\psi\rangle_+^{(\gamma)} \propto |\zeta_2\rangle + |-\zeta_2\rangle e^{i2\gamma}$ as a function of γ. The Wigner function gradually transforms from the even into the odd superposition. The detection probabilities change accordingly. We choose $|\zeta_2| = 1.67(7)$ consistent with Fig. 2(c). The error bars for $|N_+^{(\gamma)}|^2$ denote the 68% confidence interval.

In Fig. 6, we show the herald probability $|N_+^{(\gamma)}|^2$ and the resulting Wigner functions when changing the relative phase of the probability amplitude γ.

5. Measuring the variance of squeezed superpositions

To estimate the variance in Fig. 3(d) based on the experimentally reconstructed Wigner function W, we estimate the probability distribution P_x and P_p, which can be found by integrating the Wigner function along the orthogonal quadratures p and x, respectively,

$$P_x(x) = \int W(x,p)dp, \tag{A16}$$

$$P_p(p) = \int W(x,p)dx. \tag{A17}$$

The variances are then

$$\mathrm{Var}(\hat{x}) = \langle \hat{x}^2 \rangle - \langle \hat{x} \rangle^2, \tag{A18}$$

$$\mathrm{Var}(\hat{p}) = \langle \hat{p}^2 \rangle - \langle \hat{p} \rangle^2, \tag{A19}$$

where the moments of x and p are given by

$$\langle \hat{x}^k \rangle = \int x^k P_x(x)dx, \tag{A20}$$

$$\langle \hat{p}^k \rangle = \int p^k P_p(p)dp. \tag{A21}$$

For the experimental data, we rotate the matrix representing the discretized Wigner function such that the principle axes are aligned with x and p. For the simulated data, we extract a discretized Wigner function before performing the same analysis. We calculate the probability distributions and the moments by approximating the integration via the trapezoidal rule.

6. Application to other experimental platforms

The techniques presented in this work rely on two experimental capabilities: (i) the ability to engineer two SDFs to realize a nonlinear spin-dependent interaction, as described in Eq. (A1), which requires coherent control over both red-sideband (Jaynes-Cummings) and blue-sideband (anti-Jaynes-Cummings) interactions; and (ii) the ability to perform midcircuit spin measurements without destroying the quantum state of the coupled oscillator.

These requirements are met in several quantum platforms. Superconducting circuits (circuit QED), optomechanical systems, and nitrogen vacancy centers coupled to mechanical resonators can realize both red- and blue-sideband interactions via parametric driving and typically offer high-fidelity control and readout schemes.

In contrast, traditional cavity QED systems operating in the weak coupling regime [62], where an atom interacts with a high-Q microwave cavity mode, are typically described by the Jaynes-Cummings Hamiltonian under the rotating-wave approximation [63]. These systems do not naturally support the anti-Jaynes-Cummings interaction required for our method and, as a consequence, make it challenging to implement the SDFs necessary to achieve the nonlinear spin-dependent interaction.

However, there exists a scheme discussed in Ref. [55], which relies on a coherent photon state being reflected from a cavity coupled to an atom. In such a setup, the cavity imparts a conditional π phase shift depending on the atomic state, flipping the sign of the optical field, thus turning a coherent state $|\alpha\rangle$ into $|-\alpha\rangle$, enabling the generation of ordinary cat states $|\alpha\rangle \pm |-\alpha\rangle$. This scheme could be modified to use a squeezed photon state as input, which would generate optical superpositions $|\zeta\rangle \pm |-\zeta\rangle$.

APPENDIX B: EXTENDED EXPERIMENTAL DATA AND PARAMETERS

1. Experimental parameters for the results in the main text

For Figs. 2–4, we used the experimental parameters tabulated in Table I.

For Fig. 5, we use the same parameter configuration as for Fig. 2(b) and adjust the number of shots such that we have more than 300 successful heralds per point. For Fig. 6, we use the same parameter configuration as for Fig. 2(c) and adjust the number of shots such that we have more than 300 successful heralds per point.

TABLE I. Experimental parameters for Figs. 2–4. All $\hat{\sigma}_z$ interactions are embedded in a spin-echo sequence; hence, the duration t is given as $2 \times t_{\mathrm{arm}}$, where t_{arm} is the full width at half maximum duration for which the interaction is applied in each arm. We show the used power P at the ion per SDF, detuning Δ of the SDFs used to generate the interaction, the spin conditioning $\hat{\sigma}_\beta$, the approximate herald probability $p = N_{\mathrm{surv}}/N_{\mathrm{shots}}$, where the number of initial shots N_{shots} and N_{surv} the number of heralds, the estimated generalized squeezing parameter $|\zeta_k|$, and k the order of the nonlinearity. For Fig. 4, $|\zeta_1| = \Omega_\alpha t$.

Figures	P (mW)	$\Omega_\alpha, \Omega_{\alpha'}$ (2π kHz)	$\Delta/2\pi$ (kHz)	t (μs)	$\hat{\sigma}_\beta$	$p = N_{\mathrm{surv}}/N_{\mathrm{shots}}$	$\lvert\zeta_k\rvert$	k
2(a)	0.5	0.601(2), 0.608(2)	50	$2 \times$ (0–440)	$\hat{\sigma}_z$	−/300	0–2.5(1)	2
2(b), 2(h)	0.5	0.601(2), 0.608(2)	50	2×200	$\hat{\sigma}_z$	∼340/500	1.12(5)	2
2(c), 2(i)	0.5	0.601(2), 0.608(2)	50	2×300	$\hat{\sigma}_z$	∼390/1000	1.67(7)	2
2(d), 2(j)	1	0.849(3), 0.860(3)	25	500	$\hat{\sigma}_x$	∼330/400	0.74(5)	3
2(e), 2(k)	1	0.849(3), 0.860(3)	25	500	$\hat{\sigma}_x$	∼270/1000	0.74(5)	3
2(f), 2(l)	1	0.849(3), 0.860(3)	25	2×300	$\hat{\sigma}_z$	∼450/500	0.059(5)	4
2(g), 2(m)	2	1.201(4), 1.216(4)	25	2×200	$\hat{\sigma}_z$	∼160/1200	0.16(1)	4
3(c), 3(d)	0.5	0.601(2), 0.608(2)	25	200/200	$\hat{\sigma}_z$	∼340/500	1.12(5)	2
3(e)	2	1.201(4), 1.216(4)/0.363(1)	100/−25	200/200	$\hat{\sigma}_z$	∼300/400	1.12(5)/0.25(2)	2/3
4	0.5	0.608(2), 0.672(2)/-	25/0	$2 \times 100/108.6$	$\hat{\sigma}_z/\hat{\sigma}_x$	∼420/1200	1.25(4)/3.23(7)	2/1

2. Midcircuit detection error

The fidelity of the midcircuit detection directly determines the degree of certainty to which we know the heralded state. We consider the imperfect detection in the case of heralding the odd superposition $|\psi_{k,-}\rangle$. Just before detection, the wave function is

$$|\psi\rangle = N_{k,-}|\psi_{k,-}\rangle|1_s\rangle + N_{k,+}|\psi_{k,+}\rangle|0_s\rangle. \tag{B1}$$

With perfect detection, we could obtain the true description of $|\psi_{k,-}\rangle$. With detection errors, if we herald on $|1_s\rangle$ (dark), the state reads

$$\rho_{\mathrm{detect}} \propto P(\mathrm{dark}|\mathrm{dark})|N_{k,-}|^2|\psi_{k,-}\rangle\langle\psi_{k,-}| + P(\mathrm{dark}|\mathrm{bright})|N_{k,+}|^2|\psi_{k,+}\rangle\langle\psi_{k,+}|, \tag{B2}$$

where $P(\mathrm{dark}|\mathrm{dark})$ is the detection probability of dark given dark, which is the complementary event of $P(\mathrm{bright}|\mathrm{dark})$ (false bright) and $P(\mathrm{dark}|\mathrm{bright})$ the probability of dark given bright (false dark). Hence, the ratio of the mixture m of making the desired state to the false dark state is given by

$$m = \frac{P(\mathrm{dark}|\mathrm{dark})|N_{k,-}|^2}{P(\mathrm{dark}|\mathrm{bright})|N_{k,+}|^2} \approx \frac{|N_{k,-}|^2}{P(\mathrm{dark}|\mathrm{bright})|N_{k,+}|^2}. \tag{B3}$$

In Fig. 7, we measure and fit the histograms of our detection sequence. From the fits (see Fig. 8), we estimate the false dark probability to be $P(\mathrm{dark}|\mathrm{bright}) = 4.9 \times 10^{-5}$. For the interactions considered the true herald ratio $|N_{k,-}|^2/|N_{k,+}|^2 \geq 0.1$. Hence, given our readout

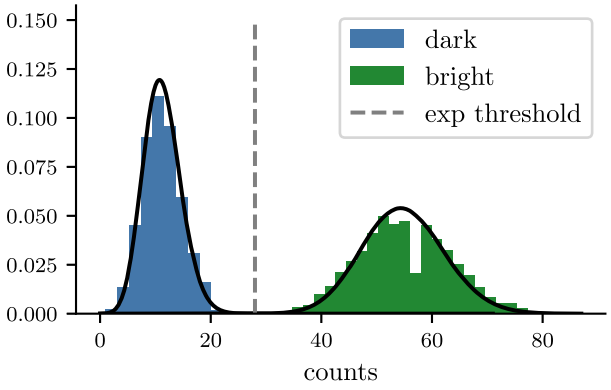


FIG. 7. Histogram of the fluorescence counts during a readout sequence (200 μs) when preparing the spin in $|1_s\rangle$ (dark) or $|0_s\rangle$ (bright). The black line denotes fits to a Poisson distribution with an expected count of 11.24 and 54.82, respectively. The experimental threshold was set to 28 counts.

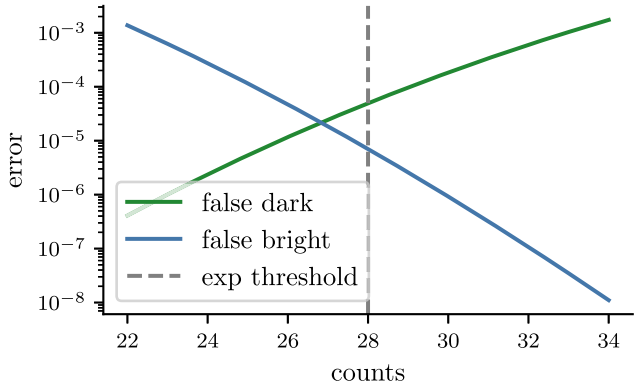


FIG. 8. Cumulative error probability of the Poisson fits in Fig. 7. The left tail of the bright distribution leads to false dark counts $P(\mathrm{dark}|\mathrm{bright})$. The right tail of the dark distribution leads to false bright counts $P(\mathrm{bright}|\mathrm{dark}) = 1 - P(\mathrm{dark}|\mathrm{dark})$. With the experimental threshold of 28 counts, we have false dark and false bright probabilities of 4.9×10^{-5} and 7.0×10^{-6}, respectively. In practice, the false bright probability is dominated by the finite lifetime of the dark state (approximately 0.4 s), which at a readout duration of 200 μs leads to an error of order $\sim[(200\ \mu\mathrm{s})/(0.4\ \mathrm{s})] = 5 \times 10^{-4}$.

errors, the resulting $m > 10^3$. If the true herald ratio is even lower, the experimental threshold can be adjusted at the expense of a small loss in overall detection events. We can also measure a cumulative state preparation and readout error by calculating the dark and bright probability based on the actual histogram data. We find $P(\text{dark}) = 0.993$. Hence, the probability of preparing and measuring dark is dominated by the state preparation process.

Another error contribution in our experiment was leakage of the 1033-nm deshelving laser. This results in a decay of the excited $|1_s\rangle$ state that is faster than the lifetime of the transition. This leakage is observed in the baseline measurement of Fig. 2(a) (green crosses). At 880 μs, we observe a contrast loss of approximately 5%. This could be resolved by improving the extinction of the 1033 nm when it is switched off.

3. Effect of midcircuit detection on ion motion

We verify that performing a midcircuit detection on a dark state ($|1_s\rangle$) leaves the motional state unperturbed. We first prepare a regular squeezed state $|\zeta_2, 1_s\rangle$, followed by the midcircuit readout before finally measuring the characteristic function along the principle axes of the squeezed state. We investigate three different versions of the midcircuit measurement: regular measurement (i.e., collect fluorescence for 200 μs), adding 200 μs delay, but not applying the fluorescence laser, and omitting the midcircuit measurement altogether. The measurement of the characteristic function for the three different settings is

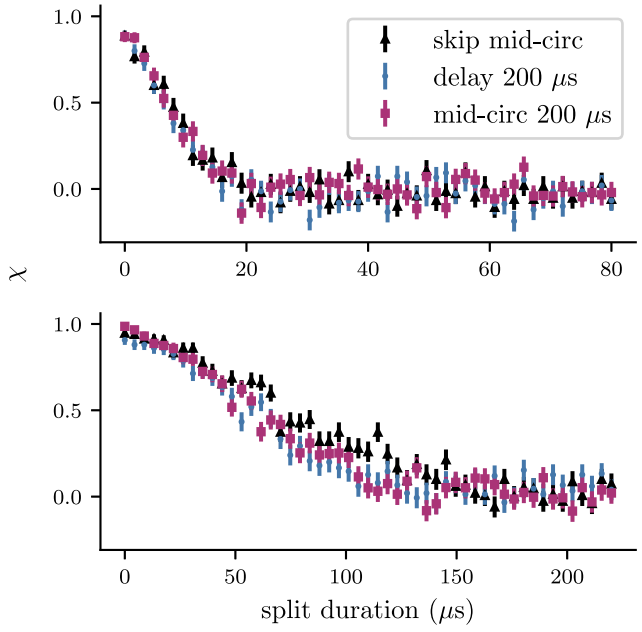


FIG. 9. Real part of the characteristic function χ along the two principal axes of a squeezed state. In these experiments, we create a squeezed state before applying a spin-dependent force for a variable duration along each of the principal axes. We include three different versions of the midcircuit operation: the full measurement, a 200 μs delay, and skipping this step altogether. Along the squeezed axis, the three settings do not differ. Along the antisqueezed axis, the two settings that increase the sequence length by 200 μs decay a bit faster. This faster decay is a result of the non-negligible heating effects and is discussed in Ref. [33]. The error bars denote the 68% confidence intervals.

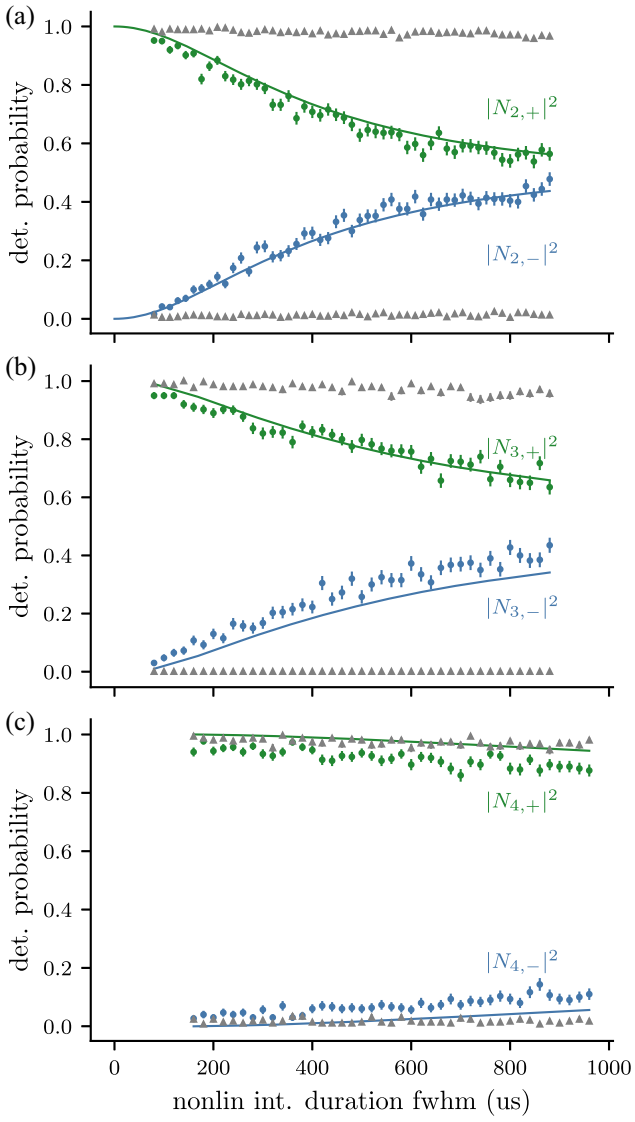


FIG. 10. Probabilities of detecting the even ($|N_{k,+}|^2$, blue) and odd ($|N_{k,-}|^2$, green) superpositions $|\psi_{k,\pm}\rangle = 1/(2N_{k,\pm}) \cdot (|\zeta_k\rangle \pm |-\zeta_k\rangle)$ as a function of the interaction duration. We present the data for $k = 2$ (a), $k = 3$ (b), and $k = 4$ (c) for squeezing, trisqueezing, and quadsqueezing, respectively. The theoretical detection probability values $|N_{2,\pm}|^2$ predicted by the coefficients in Eq. (2) are displayed as solid lines in (a). (b),(c) The solid lines represent the numerical prediction of $|N_{k,\pm}|^2$. Triangles denote the baseline where the system is left idle for the same duration as the nonlinear interaction is applied. The error bars denote the 68% confidence interval. (a) Identical to Fig. 2(a) if the x axis is rescaled to $|\zeta_2| = \Omega_2 t_{\text{FWHM}}$.

shown in Fig. 9. We conclude that the midcircuit measurement does not perturb the motional state beyond increasing the sequence length by the midcircuit measurement duration.

4. Detection probabilities for equal superpositions shown in Fig. 2

We repeat the detection probability measurements shown in Fig. 2(a) for the tri- and quadsqueezed superpositions (see Fig. 10). A closed-form analytic solution does not exist for these superpositions [34]; we replace the theory line with a numerically simulated curve. We compare the detection probabilities of these superpositions to the probabilities obtained when no interaction is applied (i.e., system left idle). Especially for the quadsqueezed state, the change in probability from leaving the system idle becomes comparable to the detection probability. This explains why the quadsqueezed superposition substantially deviates from the numerical prediction.

APPENDIX C: CHARACTERIZING THE SUPERPOSITIONS

1. Fidelity estimation

To quantify the closeness between continuous-variable quantum states, we follow the theoretical framework established in Ref. [64]. A common metric is the Uhlmann-Jozsa fidelity,

$$F_1(\rho,\sigma) = \left(\mathrm{Tr}\sqrt{\sqrt{\rho}\sigma\sqrt{\rho}}\right)^2. \tag{C1}$$

In the special case where at least one of the states is pure, this expression simplifies to

$$F_1(\rho,\sigma) = \mathrm{Tr}(\rho\sigma). \tag{C2}$$

However, the general expression is computationally expensive and often impractical when dealing with experimentally reconstructed mixed states.

As an alternative, we consider the Hilbert-Schmidt fidelity,

TABLE II. Extracted fidelity F_2 between experimental and numerically simulated Wigner functions.

Figures	F_2
2(b), 2(h)	0.98
2(c), 2(i)	0.71
2(d), 2(j)	0.91
2(e), 2(k)	0.57
2(f), 2(l)	0.94
2(g), 2(m)	0.29
3	0.83
4	0.87

TABLE III. Fidelity F_2 for both the simulated and the experimentally measured states to the ideal pure state in Fig. 12.

	Even	Odd
$F_2^{\text{exp -ideal}}$	0.71	0.28
$F_2^{\text{num-ideal}}$	0.71	0.32

$$F_2(\rho,\sigma) = \frac{\mathrm{Tr}(\rho\sigma)}{\max\left(\mathrm{Tr}(\rho^2),\mathrm{Tr}(\sigma^2)\right)}, \tag{C3}$$

which serves as a computationally efficient proxy. This quantity is particularly useful when the states are represented via Wigner functions, as the trace overlap can be computed using phase-space integrals,

$$\mathrm{Tr}(\rho\sigma) = 2\pi \int dxdp W_\rho(x,p) W_\sigma(x,p). \tag{C4}$$

The fidelities $F_1(\rho,\sigma)$ and $F_2(\rho,\sigma)$ coincide when at least one of the two states is pure. When both states are mixed, the relationship between F_1 and F_2 is more subtle and should be interpreted accordingly. The properties, advantages, and limitations of F_2 are discussed in detail in Ref. [64].

In our work, we use F_2 quantify the agreement between experimentally reconstructed and numerically simulated Wigner functions for the states shown in Figs. 2–5, as summarized in Table II. Additionally, we compute F_2 to assess the closeness of both the simulated and the experimentally measured states to the ideal pure state, as illustrated in Fig. 12 and summarized in Table III. Additionally, we compute F_2 to assess the closeness of both the simulated and the experimentally measured states

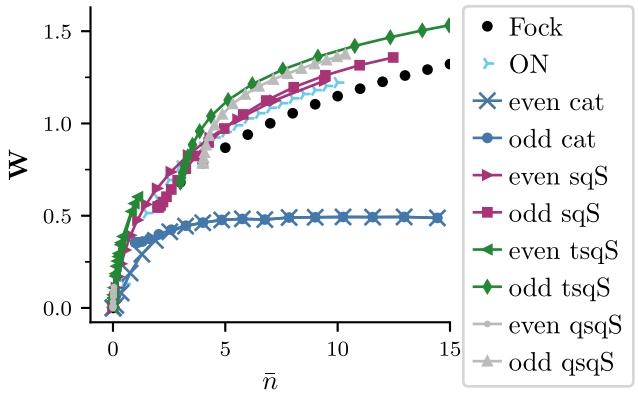


FIG. 11. Wigner logarithmic negativity **W** for the states synthesized in this article as a function of mean phonon number $\bar{n} = \langle N\rangle_{\text{osc}}$. We calculate **W** via numerical simulation assuming a perfect noiseless system with an initial oscillator state with $\bar{n} = 0$ (i.e., perfect ground state) and no heating. We estimate **W** for Fock states, Fock-state superpositions $|0_{\text{osc}}\rangle + i|N_{\text{osc}}\rangle$ (ON), cat states, squeezed superpositions (sqS), trisqueezed superpositions (tsqS), and the quadsqueezed superpositions (qsqS). The superpositions exhibit **W** exceeding the Fock and ON states for the same $\bar{n}$.

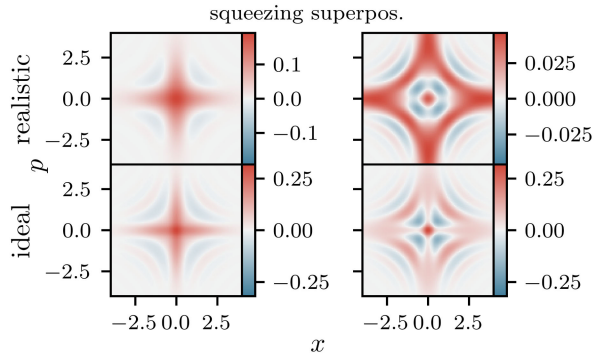


FIG. 12. Wigner function for squeezing assuming either an ideal system or considering realistic system parameters (starting state $\bar{n} = 0.1$ and heating rate of $\dot{\bar{n}} = 300$ quanta/s).

to the ideal pure state, as illustrated in Fig. 12 and summarized in Table III. This second application provides a conservative estimate of fidelity, since we do not account for any of the known noise sources in our system. Here, F_2 coincides with the Uhlmann-Jozsa fidelity F_1 as the ideal state is pure.

2. Wigner negativity of different ideal superpositions

There are several measures to quantify the utility, or more precisely, the resourcefulness of the oscillator-state superpositions. Here, we choose the Wigner logarithmic negativity [29,30]

$$\mathbf{W}(\rho) = \log\left(\int dxdp|W_\rho(x,p)|\right), \tag{C5}$$

where W is the Wigner function of state ρ. WLN is a resource monotone, but it is still an active area of research under which circumstances it adequately quantifies the difficulty of simulating the state classically. We calculate the expected WLN $\mathbf{W}$ of the ideal version of the equal superposition states studied in this work (coherent, squeezed, and trisqueezed superpositions) and pure Fock states using a discrete version of Eq. (C5). We calculate the negativity for each oscillator state as a function of the mean phonon number $\bar{n} = \langle\hat{N}\rangle_{\mathrm{osc}}$, as shown in Fig. 11.

3. Comparing the realistic and ideal states

While we have good agreement between experiment and numerical simulation with realistic system parameters, i.e., finite initial oscillator occupation of $\bar{n} = 0.1$ and non-negligible heating rate of $\dot{\bar{n}} = 300$ quanta/s, there is a difference compared to an ideal system with perfect initial ground state and no heating rate. The macroscopic properties, such as the overall shape of the Wigner function, stay the same, but certain details or features become more or less accentuated. We qualitatively compare the realistic and ideal states in Fig. 12. The Wigner functions with finite temperature and heating effects are identical to the plots shown for Figs. 2(h) and 2(i).

TABLE IV. Extracted Wigner logarithmic negativities and minimum negative value of the Wigner function $\min(W)$ reached for the squeezed superposition. We compare the experimental reconstructed, realistic simulation, and ideal simulation for both even and odd superposition states.

Squeezed superposition	WLN	$\min(W)$
Even: exp	0.14	−0.025
Even: realistic	0.132	−0.022
Even: ideal	0.408	−0.050
Odd: exp	0.209	−0.025
Odd: realistic	0.193	−0.025
Odd: ideal	0.756	−0.177

We extract the WLN described in the previous section for the numerically simulated and experimentally reconstructed states. The WLN for the experimental states is close to the value of the realistic simulation, but reduced compared to the ideal states due to experimental imperfections. We present the extracted values in Table IV. However, we emphasize that these values should give a qualitative estimation, but do not represent a quantitative characterization. We would need to improve the Wigner function reconstruction protocol to deal with spurious ripples in the Wigner function for larger x, p values, which arise due to shot noise and other experimental imperfections during the tomography. We have windowed the Wigner function around the origin to avoid biasing the results. The window size is set such that $[\int_{\mathrm{window}} W(x,p)dxdp]/[\int W(x,p)dxdp] = 0.95$. For reference, we also extract the minimum value of the Wigner function $\min(W)$, which is occasionally stated in the literature. However, we stress that this measure is bounded to $\min(W) \geq -1/\pi$ and confirms only that the state has Wigner negativity, but does not measure resourcefulness. For example, the ideal Fock state $|1\rangle$ has a minimum value of $\min(W) = -1/\pi$.

4. Reconstruction of the Wigner function

We obtain the Wigner function via Fourier transform of the characteristic function $\chi(\beta) \in \mathbb{C}$, following Refs. [33,41]. As an example, we provide the characteristic function of the even [Fig. 2(b)] and odd squeezed superposition states [Fig. 2(c)]. In Fig. 13, we show the experimentally measured characteristic function. In the experimentally measured characteristic function, and consequently, in the reconstructed Wigner function, we find a tilt relative to the x, p axes of approximately 0.44 rad, with daily variations on the order of 0.06 rad. This tilt is the result of a constant motional phase offset between the SDF used for reconstruction and the axis of the squeezing interaction. To make the comparison to the numerically simulated data easier, we correct the shift by digitally rotating the reconstructed Wigner function by this amount.

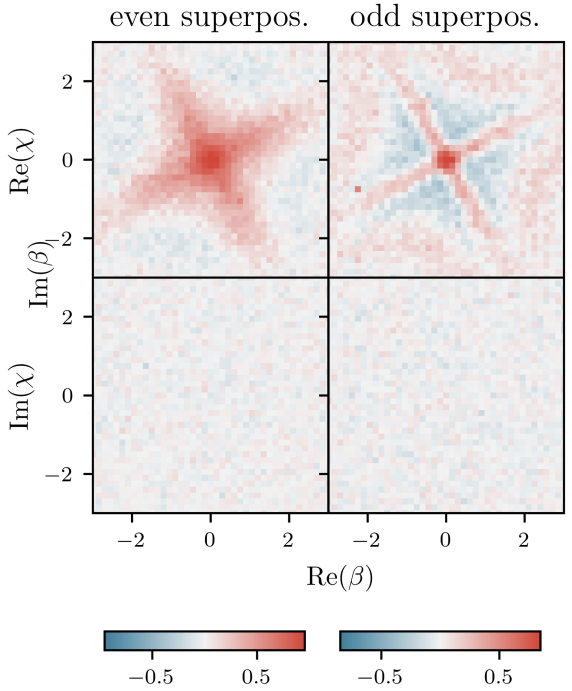


FIG. 13. Characteristic function of Figs. 2(b) and 2(c). The imaginary part $\mathrm{Im}[\chi(\beta)]$ vanishes despite the Wigner function's complex pattern.

5. Density matrices of equal superpositions in Fig. 2

To provide more intuition about the odd and even superposition states, we show the density matrices in the Fock basis (see Fig. 14). As expected, only the Fock states $|k \cdot 2n\rangle$ for the even superpositions and $|k \cdot (2n+1)\rangle$ for the odd superpositions, where $n \in \mathbb{N}_0$ and k the order of the nonlinear interaction, are populated.

6. Superpositions as logical code words

The difference in distribution of Fock states between even and odd states could allow us to assign logical code words of the form

$$|0_L^{(k)}\rangle = \sum_{n=0}^{\infty} a_n |k \cdot 2n\rangle, \tag{C6}$$

$$|1_L^{(k)}\rangle = \sum_{n=0}^{\infty} a_n |k \cdot (2n+1)\rangle. \tag{C7}$$

For example, for $k = 1$ and suitable a_n, this describes the two-component cat-state code, whereas for $k \geq 2$ it describes the superposition states produced in Fig. 2. As discussed in Ref. [32], a useful operator basis for errors is given by

$$\hat{E}_j(\theta) := \begin{cases} e^{i\theta\hat{n}}\hat{a}^{|j|}, & \text{for } j < 0, \\ (\hat{a}^\dagger)^{|j|} e^{i\theta\hat{n}}, & \text{for } j \geq 0. \end{cases} \tag{C8}$$

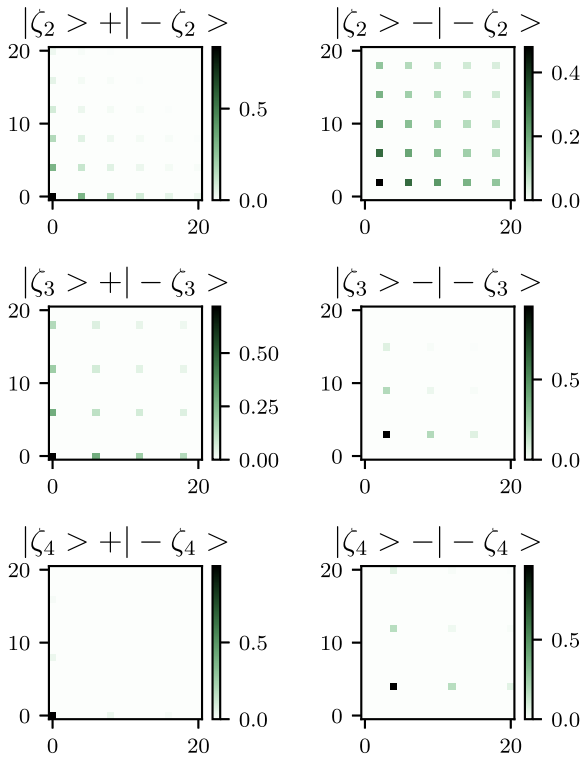


FIG. 14. Visual representation of the first 20×20 entries of the density matrices expressed in the Fock-state basis for squeezed, trisqueezed, and quadsqueezed superpositions shown in Fig. 2 assuming a perfect ground state $|0_{\mathrm{osc}}\rangle$, i.e., $\bar{n} = 0.0$ and no decoherence effects. We assumed squeezing magnitudes $\zeta_2 = \{1.12(5), 1.67(7)\}$, $\zeta_3 = \{0.74(5), 0.74(5)\}$, and $\zeta_4 = \{0.059(5), 0.16(1)\}$ as in Fig. 2.

Thus, an error $\hat{E}_j^{(\theta)}$ with $0 < |j| < k$ is detectable. This follows from the Fock-space separation of k quanta between the code words $|0_N\rangle$ and $|1_N\rangle$, e.g.,

$$\langle 1_L^{(k)} | \hat{E}_j(\theta) | 0_L^{(k)} \rangle = 0. \tag{C9}$$

[1] E. Schrödinger, *Die gegenwärtige Situation in der Quantenmechanik*, Naturwissenschaften **23**, 807 (1935).
[2] C. L. Degen, F. Reinhard, and P. Cappellaro, *Quantum sensing*, Rev. Mod. Phys. **89**, 035002 (2017).
[3] A. D. Ludlow, M. M. Boyd, J. Ye, E. Peik, and P. O. Schmidt, *Optical atomic clocks*, Rev. Mod. Phys. **87**, 637 (2015).
[4] J. Preskill, *Quantum computing and the entanglement frontier*, arXiv:1203.5813.
[5] A. D. Leu, M. F. Gely, M. A. Weber, M. C. Smith, D. P. Nadlinger, and D. M. Lucas, *Fast, high-fidelity addressed single-qubit gates using efficient composite pulse sequences*, Phys. Rev. Lett. **131**, 120601 (2023).

[6] R. Barends *et al.*, *Superconducting quantum circuits at the surface code threshold for fault tolerance*, Nature (London) **508**, 500 (2014).

[7] J. Yoneda, K. Takeda, T. Otsuka, T. Nakajima, M. R. Delbecq, G. Allison, T. Honda, T. Kodera, S. Oda, Y. Hoshi, N. Usami, K. M. Itoh, and S. Tarucha, *A quantum-dot spin qubit with coherence limited by charge noise and fidelity higher than 99.9%*, Nat. Nanotechnol. **13**, 102 (2018).

[8] D. Gottesman, A. Kitaev, and J. Preskill, *Encoding a qubit in an oscillator*, Phys. Rev. A **64**, 012310 (2001).

[9] P. T. Cochrane, G. J. Milburn, and W. J. Munro, *Macroscopically distinct quantum-superposition states as a bosonic code for amplitude damping*, Phys. Rev. A **59**, 2631 (1999).

[10] M. H. Michael, M. Silveri, R. T. Brierley, V. V. Albert, J. Salmilehto, L. Jiang, and S. M. Girvin, *New class of quantum error-correcting codes for a bosonic mode*, Phys. Rev. X **6**, 031006 (2016).

[11] M. Bild, M. Fadel, Y. Yang, U. von Lüpke, P. Martin, A. Bruno, and Y. Chu, *Schrödinger cat states of a 16-microgram mechanical oscillator*, Science **380**, 274 (2023).

[12] M. Kang, H. Nuomin, S. N. Chowdhury, J. L. Yuly, K. Sun, J. Whitlow, J. Valdiviezo, Z. Zhang, P. Zhang, D. N. Beratan, and K. R. Brown, *Seeking a quantum advantage with trapped-ion quantum simulations of condensed-phase chemical dynamics*, Nat. Rev. Chem. **8**, 340 (2024).

[13] K. C. McCormick, J. Keller, S. C. Burd, D. J. Wineland, A. C. Wilson, and D. Leibfried, *Quantum-enhanced sensing of a single-ion mechanical oscillator*, Nature (London) **572**, 86 (2019).

[14] M. Kudra, M. Kervinen, I. Strandberg, S. Ahmed, M. Scigliuzzo, A. Osman, D. P. Lozano, M. O. Tholén, R. Borgani, D. B. Haviland, G. Ferrini, J. Bylander, A. F. Kockum, F. Quijandría, P. Delsing, and S. Gasparinetti, *Robust preparation of Wigner-negative states with optimized snap-displacement sequences*, PRX Quantum **3**, 030301 (2022).

[15] V. G. Matsos, C. H. Valahu, T. Navickas, A. D. Rao, M. J. Millican, X. C. Kolesnikow, M. J. Biercuk, and T. R. Tan, *Robust and deterministic preparation of bosonic logical states in a trapped ion*, Phys. Rev. Lett. **133**, 050602 (2024).

[16] E. Bimbard, N. Jain, A. MacRae, and A. I. Lvovsky, *Quantum-optical state engineering up to the two-photon level*, Nat. Photonics **4**, 243 (2010).

[17] R. L. de Matos Filho and W. Vogel, *Even and odd coherent states of the motion of a trapped ion*, Phys. Rev. Lett. **76**, 608 (1996).

[18] A. Ourjoumtsev, H. Jeong, R. Tualle-Brouri, and P. Grangier, *Generation of optical 'Schrödinger cats' from photon number states*, Nature (London) **448**, 784 (2007).

[19] D. Kienzler, C. Flühmann, V. Negnevitsky, H.-Y. Lo, M. Marinelli, D. Nadlinger, and J. P. Home, *Observation of quantum interference between separated mechanical oscillator wave packets*, Phys. Rev. Lett. **116**, 140402 (2016).

[20] R. W. Heeres, P. Reinhold, N. Ofek, L. Frunzio, L. Jiang, M. H. Devoret, and R. J. Schoelkopf, *Implementing a universal gate set on a logical qubit encoded in an oscillator*, Nat. Commun. **8**, 94 (2017).

[21] C. Flühmann, T. L. Nguyen, M. Marinelli, V. Negnevitsky, K. Mehta, and J. P. Home, *Encoding a qubit in a trapped-ion mechanical oscillator*, Nature (London) **566**, 513 (2019).

[22] P. Campagne-Ibarcq, A. Eickbusch, S. Touzard, E. Zalys-Geller, N. E. Frattini, V. V. Sivak, P. Reinhold, S. Puri, S. Shankar, R. J. Schoelkopf, L. Frunzio, M. Mirrahimi, and M. H. Devoret, *Quantum error correction of a qubit encoded in grid states of an oscillator*, Nature (London) **584**, 368 (2020).

[23] S. Konno, W. Asavanant, F. Hanamura, H. Nagayoshi, K. Fukui, A. Sakaguchi, R. Ide, F. China, M. Yabuno, S. Miki, H. Terai, K. Takase, M. Endo, P. Marek, R. Filip, P. van Loock, and A. Furusawa, *Logical states for fault-tolerant quantum computation with propagating light*, Science **383**, 289 (2024).

[24] B. C. Sanders, *Superposition of two squeezed vacuum states and interference effects*, Phys. Rev. A **39**, 4284 (1989).

[25] Y. A. Barbosa, G. Marques, and B. Baseia, *Generalized superposition of two squeezed states: Generation and statistical properties*, Physica (Amsterdam) **280A**, 346 (2000).

[26] F. Nicacio, R. N. Maia, F. Toscano, and R. O. Vallejos, *Phase space structure of generalized Gaussian cat states*, Phys. Lett. A **374**, 4385 (2010).

[27] P. McConnell, A. Ferraro, and R. Puebla, *Multi-squeezed state generation and universal bosonic control via a driven quantum Rabi model*, arXiv:2209.07958.

[28] M. Ayyash, X. Xu, S. Ashhab, and M. Mariantoni, *Driven multiphoton qubit-resonator interactions*, Phys. Rev. A **110**, 053711 (2024).

[29] F. Albarelli, M. G. Genoni, M. G. A. Paris, and A. Ferraro, *Resource theory of quantum non-Gaussianity and Wigner negativity*, Phys. Rev. A **98**, 052350 (2018).

[30] R. Takagi and Q. Zhuang, *Convex resource theory of non-Gaussianity*, Phys. Rev. A **97**, 062337 (2018).

[31] M. Drechsler, M. Belén Farías, N. Freitas, C. T. Schmiegelow, and J. P. Paz, *State-dependent motional squeezing of a trapped ion: Proposed method and applications*, Phys. Rev. A **101**, 052331 (2020).

[32] A. L. Grimsmo, J. Combes, and B. Q. Baragiola, *Quantum computing with rotation-symmetric bosonic codes*, Phys. Rev. X **10**, 011058 (2020).

[33] O. Băzăvan, S. Saner, D. J. Webb, E. M. Ainley, P. Drmota, D. P. Nadlinger, G. Araneda, D. M. Lucas, C. J. Ballance, and R. Srinivas, *Squeezing, trisqueezing, and quadsqueezing in a spin-oscillator system*, arXiv:2403.05471.

[34] S. L. Braunstein and R. I. McLachlan, *Generalized squeezing*, Phys. Rev. A **35**, 1659 (1987).

[35] R. Sutherland and R. Srinivas, *Universal hybrid quantum computing in trapped ions*, Phys. Rev. A **104**, 032609 (2021).

[36] C. M. Caves, *Quantum-mechanical noise in an interferometer*, Phys. Rev. D **23**, 1693 (1981).

[37] S. C. Burd, R. Srinivas, J. J. Bollinger, A. C. Wilson, D. J. Wineland, D. Leibfried, D. H. Slichter, and D. T. C. Allcock, *Quantum amplification of mechanical oscillator motion*, Science **364**, 1163 (2019).

[38] C. W. S. Chang, C. Sabín, P. Forn-Díaz, F. Quijandría, A. M. Vadiraj, I. Nsanzineza, G. Johansson, and C. M. Wilson, *Observation of three-photon spontaneous parametric down-conversion in a superconducting parametric cavity*, Phys. Rev. X **10**, 011011 (2020).

[39] A. M. Eriksson, T. Sépulcre, M. Kervinen, T. Hillmann, M. Kudra, S. Dupouy, Y. Lu, M. Khanahmadi, J. Yang, C. C. Moreno, P. Deslsing, and S. Gasparinetti, *Universal control of a bosonic mode via drive-activated native cubic interactions*, Nat. Commun. **15**, 2512 (2024).

[40] Throughout the main text, we assume all interactions are conditioned on $\hat{\sigma}_z$. See Appendixes for the native sequences.

[41] C. Flühmann and J. P. Home, *Direct characteristic-function tomography of quantum states of the trapped-ion motional oscillator*, Phys. Rev. Lett. **125**, 043602 (2020).

[42] V. Schäfer, *Fast gates and mixed-species entanglement with trapped ions*, Ph.D. thesis, University of Oxford, 2018.

[43] K. Thirumalai, *High-fidelity mixed species entanglement of trapped ions*, Ph.D. thesis, University of Oxford, 2019.

[44] A. Mari and J. Eisert, *Positive Wigner functions render classical simulation of quantum computation efficient*, Phys. Rev. Lett. **109**, 230503 (2012).

[45] O. Hahn, R. Takagi, G. Ferrini, and H. Yamasaki, *Classical simulation and quantum resource theory of non-Gaussian optics*, Quantum **9**, 1881 (2025).

[46] While WLN is a resource monotone, it is still an active area of research under which circumstances it adequately quantifies the difficulty of simulating the state classically.

[47] The treatment can be reduced to the subspace $\{|0_s\rangle, |2_s\rangle\}$ because the interaction commutes with the computational basis and hence does not cross-couple the levels.

[48] This sequence can be understood as a Ramsey spin-echo sequence on the subsystem $\{|0_s\rangle, |2_s\rangle\}$ and, indeed, protects us against uncontrolled frequency shifts between the sublevels too.

[49] To avoid any difference in frequency shift on the subsystem between the two applied nonlinear interactions, we keep the power and detunings of the generating SDFs fixed and vary only the degree to which they do not commute (see Appendixes).

[50] K. A. Gilmore, M. Affolter, R. J. Lewis-Swan, D. Barberena, E. Jordan, A. M. Rey, and J. J. Bollinger, *Quantum-enhanced sensing of displacements and electric fields with two-dimensional trapped-ion crystals*, Science **373**, 673 (2021).

[51] Y. Liu, S. Singh, K. C. Smith, E. Crane, J. M. Martyn, A. Eickbusch, A. Schuckert, R. D. Li, J. Sinanan-Singh, M. B. Soley, T. Tsunoda, I. L. Chuang, N. Wiebe, and S. M. Girvin, *Hybrid oscillator-qubit quantum processors: Instruction set architectures, abstract machine models, and applications*, PRX Quantum **7**, 010201 (2026).

[52] F. R. Cardoso, D. Z. Rossatto, G. P. L. M. Fernandes, G. Higgins, and C. J. Villas-Boas, *Superposition of two-mode squeezed states for quantum information processing and quantum sensing*, Phys. Rev. A **103**, 062405 (2021).

[53] A. Wallraff, D. I. Schuster, A. Blais, L. Frunzio, R.-S. Huang, J. Majer, S. Kumar, S. M. Girvin, and R. J. Schoelkopf, *Strong coupling of a single photon to a superconducting qubit using circuit quantum electrodynamics*, Nature (London) **431**, 162 (2004).

[54] T. Delord, P. Huillery, L. Nicolas, and G. Hétet, *Spin-cooling of the motion of a trapped diamond*, Nature (London) **580**, 56 (2020).

[55] B. Hacker, S. Welte, S. Daiss, A. Shaukat, S. Ritter, L. Li, and G. Rempe, *Deterministic creation of entangled atom–light Schrödinger-cat states*, Nat. Photonics **13**, 110 (2019).

[56] A. M. Kaufman, B. J. Lester, and C. A. Regal, *Cooling a single atom in an optical tweezer to its quantum ground state*, Phys. Rev. X **2**, 041014 (2012).

[57] S. Nimmrichter and K. Hornberger, *Macroscopicity of mechanical quantum superposition states*, Phys. Rev. Lett. **110**, 160403 (2013).

[58] R. Penrose, *On Gravity's role in Quantum State Reduction*, Gen. Relativ. Gravit. **28**, 581 (1996).

[59] D. Stoler, *Equivalence classes of minimum uncertainty packets*, Phys. Rev. D **1**, 3217 (1970).

[60] H. P. Yuen, *Two-photon coherent states of the radiation field*, Phys. Rev. A **13**, 2226 (1976).

[61] C. Weedbrook, S. Pirandola, R. García-Patrón, N. J. Cerf, T. C. Ralph, J. H. Shapiro, and S. Lloyd, *Gaussian quantum information*, Rev. Mod. Phys. **84**, 621 (2012).

[62] S. Haroche and J.-M. Raimond, *Exploring the Quantum: Atoms, Cavities, and Photons* (Oxford University Press, New York, 2006).

[63] D. D. Bernardis, A. Mercurio, and S. D. Liberato, *Tutorial on nonperturbative cavity quantum electrodynamics: Is the Jaynes-Cummings model still relevant?*, J. Opt. Soc. Am. B **41**, C206 (2024).

[64] Y.-C. Liang, Y.-H. Yeh, P. E. M. F. Mendonça, R. Y. Teh, M. D. Reid, and P. D. Drummond, *Quantum fidelity measures for mixed states*, Rep. Prog. Phys. **82**, 076001 (2019).